(Preprint) AAS 13-279

ATMOSPHERIC DENSITY RECONSTRUCTION USING SATELLITE ORBIT TOMOGRAPHY

Michael A. Shoemaker[*], Brendt Wohlberg[†], and Josef Koller[‡]

Improved thermospheric neutral density models are required to better predict LEO satellite orbits. This research describes a new method to estimate the density using a tomography-based approach, where the orbit states of satellites serve as the measurements. The variational equation for the semimajor axis due to perturbing drag acceleration is used to relate the change in osculating specific mechanical energy of the orbit to the integrated density over the orbit. Using several such measurements from a number of satellites, one can estimate the density scale factor (i.e. a correction to an assumed density model). The problem considered here uses measurements from 100 satellites and solves for the spatially resolved global density scale factor discretized over 324 grid elements spanning 300 to 500 km altitude. This ill-posed problem is solved using Tikhonov regularization, with the 3D gradient chosen as the regularization operator, resulting in a penalty on the spatial smoothness of the estimated density. Preliminary simulation results show that the true time-averaged density can be reconstructed to within approximately 10%, using only simulated ground-based tracking measurements separated over 5 orbital revolutions.

INTRODUCTION

Inaccurate atmospheric drag models are the largest remaining error source affecting orbit prediction accuracy for most low-Earth orbit (LEO) satellites. Error in the modeled atmospheric density is a major contributing factor. Several authors[1,2] have noted that little progress had been made in reducing the errors in modeled density from the 1960s until recently, during which time errors of 15% or more were common. Drag models errors of this magnitude can result in predicted satellite position errors on the order of 1 km or more after a single day.[3,4] There has thus been much research attention in recent years on further improving density modeling for drag estimation.

Some examples of papers that give a good overview of the history and recent advancements in density modeling using satellite measurements include Refs. 2, 3, and 5. Broadly speaking, methods of estimating atmospheric density can be divided into those that use the motion of the satellite in the atmosphere, and those that use remote sensing methods (e.g. onboard spectroscopic sensing of upper atmospheric airglow[6]). The methods based on satellite motion can be further categorized into two groups: (1) those using tracking measurements, usually ground-based, of a

[*]Postdoctoral Research Associate, Space Science and Applications (ISR-1), Los Alamos National Laboratory, P.O. Box 1663, Mail Stop D466, Los Alamos, NM.

[†]Staff Scientist, Applied Mathematics and Plasma Physics (T-5), Los Alamos National Laboratory, P.O. Box 1663, Los Alamos, NM.

[‡]Staff Scientist, Space Science and Applications (ISR-1), Los Alamos National Laboratory, P.O. Box 1663, Mail Stop D466, Los Alamos, NM.

large number of satellites, (2) and those using specialized onboard measurements, such as high-accuracy accelerometers and GPS receivers, on a small number of satellites.

Satellites with specialized onboard instruments have provided much useful data on density modeling. For example, the CHAMP and GRACE satellites are equipped with accelerometers and high-precision orbit estimation systems (e.g. GPS), which allow nearly continuous measurements of drag accelerations.[7–10] Because the other factors that affect drag are fairly well known for these satellites (mass, area, drag coefficient), the local density can be accurately estimated along the orbit. For example, McLaughlin et al.[4] demonstrated a sequential estimation scheme to estimate simultaneously the density and ballistic coefficient using high precision orbit ephemerides from the CHAMP satellite. A disadvantage of these approaches is that they are limited to a small number of specialized missions, making it difficult to apply the results to a global density model correction.

The other category, using tracking measurements (e.g. ground-based radar and optical) is often called the Dynamic Calibration of the Atmosphere (DCA) method, because they estimate corrections to a given density model. Thus, in contrast with the accelerometer methods described above, this category uses sparse measurements having lower accuracy, but on a larger set of satellites. Much work in this area has been performed by the U.S. Air Force in support of its High Accuracy Satellite Drag Model (HASDM),[11–16] which uses tracking measurements to estimate a correction to the Jacchia 70 empirical density model. Corrections to the exospheric and inflection point temperatures in the vertical temperature profile are represented as two separate spherical harmonic expansions, varying in the literature from second degree and order[13] up to a 4×0 expansion.[15] Sutton et al.[16] improved on this method by using a different set of basis functions to compute the temperature corrections. The number of tracked objects used by HASDM varies in the literature as well, but has ranged from around 70 satellites[12] up to 144 satellites.[15] Accurate estimates of the ballistic coefficients for the target calibration satellites are required.[11] These target satellites are tracked multiple times per orbital revolution[12] by the Space Surveillance Network of radar and optical sensors,[17] and a weighted least squares differential correction method is used across all targets that simultaneously solves for the density corrections and a state vector for each target.[14] The final estimated density corrections, in the form of 3-hour fits to the data, are claimed to be within a few percent of the true density.[14]

The contribution of the present paper is the description of a new method, inspired by tomography, to correct atmospheric density models . Tomography is an inverse problem, with various applications in science and engineering, involving the infererence of the properties of the material within a body using only measurements taken external to the body.[18] A good example is X-ray computed tomography (CT) widely used in medical imaging (Figure 1). Here, X-rays with known intensities are emitted at various angles through a patient's body, where the final intensities of the rays are measured at a detector on the opposite side of the body. Let $f(x)$ be the X-ray attenuation coefficient of the tissue at point x, then an X-ray traveling a distance Δx will have a relative intensity loss of[19]

$$\frac{\Delta I}{I} = f(x)\Delta x. \tag{1}$$

Integrating over the ray's path yields

$$\oint \frac{dI}{I} = \oint f(x)dx, \tag{2}$$

and given the known initial intensity I_0 and measured final intensity I_1 of the ray, the above integral

becomes

$$\ln\left(I_1/I_0\right) = \oint f(x)dx. \tag{3}$$

The inverse problem then involves: (1) discretizing the volume into cells, (2) rewriting the integral in Eq. (3) as a summation, (3) collecting the cell quantities and measurement for each ray into a linear equation, and (4) solving for the discretized $f(x)$ by inversion of the resulting system of linear equations. Since $f(x)$ is related to the density of the tissue, one can then construct a map of the internal density. Note also that because the matrix normal equation in the linear system derived from Eq. (3) is often ill-posed, it is common to use regularization to stabilize the system.

Our approach is motivated by the analogy between the path of an X-ray beam through a solid object and the orbital path of a satellite through the upper atmosphere. In the case of the X-ray beam, the log of the attenuation factor is simply the integral of the attenuation coefficient along the path. At a more abstract level, a measurable quantity can be expressed as a path integral over the spatially varying quantity to be estimated. Since the state of a satellite along its orbit is continuously changing as a result of drag, which depends on the atmospheric density, we find a relationship between measurable orbital parameters and density that can be written in the form of a path integral over the density, allowing us to apply tomographic reconstruction methods.

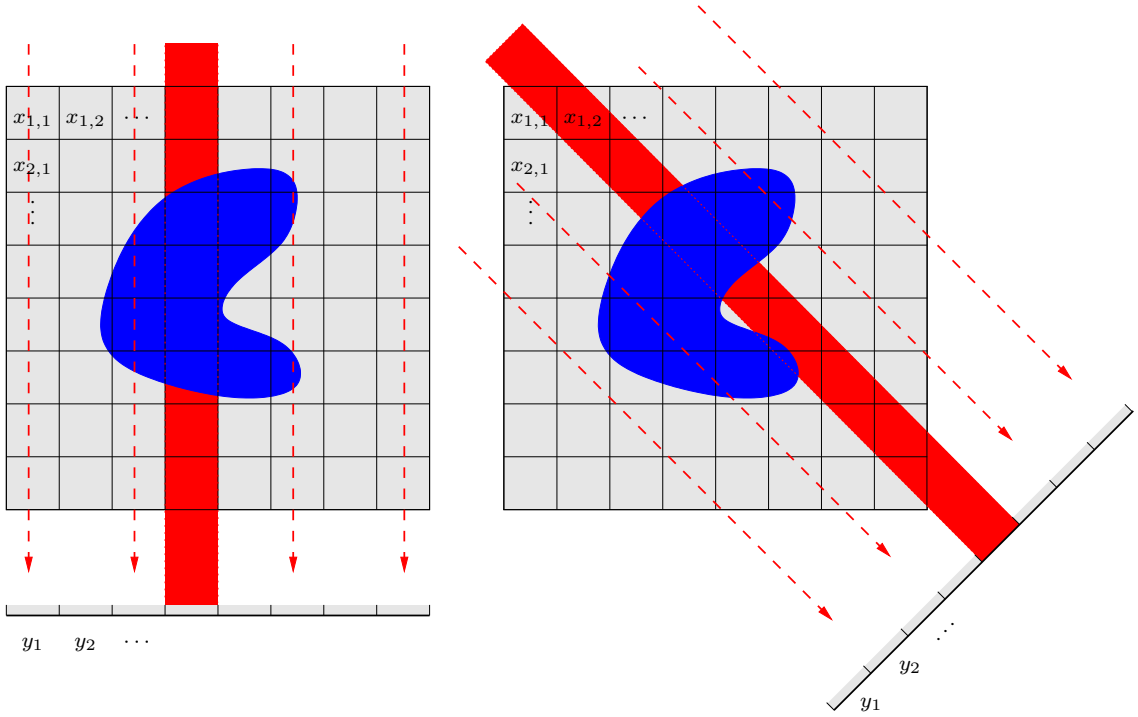

Figure 1. Illustration of standard computed tomography: the region (gray box) containing an object of interest (blue shape) is discretized into many cells, and a known beam source (e.g. X-ray) is emitted towards a sensor at various angles. The red bars indicate the relationship between a sensor element and the cells (sometimes fractional) traversed by the part of the beam detected by that sensor. This relationship determines the linear equations that connect the cell densities with the measured values for each arrangement of the sensor with respect to the density grid.

This sort of tomography approach has never been applied to satellite orbital motion to deduce atmospheric density. Several studies have used satellite-based measurements with tomography and

regularization (e.g. Refs. 20–24), but usually the measurements involve radiometric observables from specialized onboard instruments (e.g. infrared, microwave), rather than the satellite orbital elements themselves. The main advantage of the tomography approach in this paper is that sparse tracking data is assumed, in contrast to the HASDM method described above where the target satellites are tracked every revolution. Thus, it may be feasible to achieve similar results with fewer sensors.

TOMOGRAPHY APPLIED TO SATELLITE ORBITS

This section describes how the tomography method is applied to a set of satellite tracking measurements. First, a grid is defined within a certain range of radial (r), latitude (θ), and longitude (ϕ) values. For simplicity, the grid's latitude and longitude coordinates are defined in the inertial (J2000) reference frame, since the satellite positions will also be described in this frame. Thus, the grid will be nearly fixed relative to the Sun* over the time spans of interest in this study (i.e. ~ 1 day).

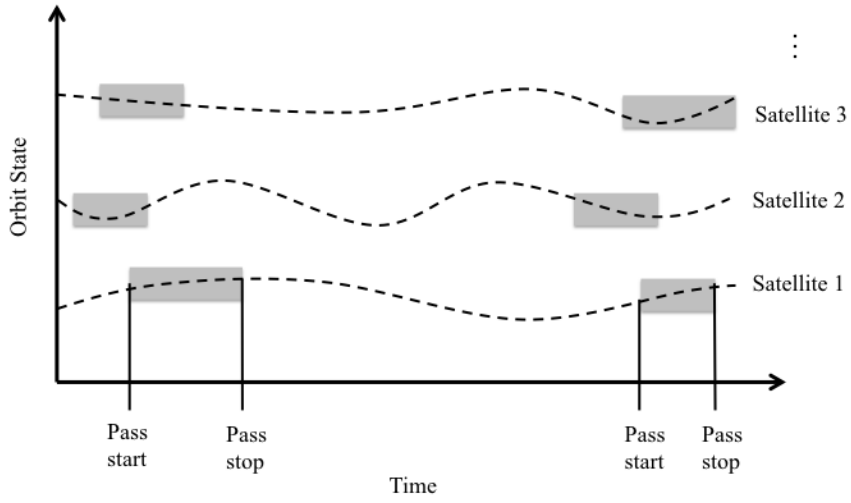

Figure 2. Sketch of orbit estimation scheme, illustrating several satellites having time-varying orbital states and being in view of ground sites at certain times (gray regions).

A set of target satellites are assumed, which have trajectories passing through the grid, either partially (e.g. an eccentric orbit with perigee falling within the grid) or in full (e.g. a nearly-circular LEO orbit). We assume that each satellite will be visible to a ground-based tracking sensor for a minimum time span of a few minutes. During this "pass", the satellite is tracked by the sensor and measurements such as range, range rate, and angles are recorded . Although the details of the given sensor and orbit estimation scheme are unimportant for the current discussion, we assume a

*The direction to the Sun will have a drift of approximately 1 degree per day in the inertial longitude direction using this grid definition. This can be alleviated in future studies by using the local solar time in place of the longitude.

sequential estimator, such that the measurements are processed and a final orbit estimate (OE) is generated at the pass stop time. This OE consists of the J2000 position and velocity vectors. The OE at the end of the first pass is then propagated to the start time of the next pass, where it is used as the initial state estimate for the second pass. The sequential estimation process then continues, processing the measurements during pass 2, and producing a new state estimate at the second pass stop time.

This sequential estimation scheme is applied to each of the satellites. The sketch in Figure 2 shows this for several satellites. Thus, for a given satellite, we will have estimates of the semimajor axis a at t_1 (pass 1 stop time), and a at t_2 (pass 2 stop time). We now treat the change in a over the time span from t_1 to t_2 to be the measurement for the tomography. The final estimated density from the tomography will effectively be an estimate of the time-average of the temporal variations of the true density. The pass times do not need to occur simultaneously for all satellites, and depending on the number of sensors and their placement, these pass times may have some variation in time. Thus, we can say that the tomography is effectively measuring the time-average density between the mean pass 1 stop time and the mean pass 2 stop time.

It is important to note that there are no constraints on the satellites' spatial position at t_1 and t_2, other than the visibility constraints of the chosen sensor geometry. For example, Satellite 1 could be observed at t_1 over the north pole, and several revolutions later it is observed at t_2 near the equator, whereas Satellite 2 could be observed at both times at the same ground station at the south pole. However, it is assumed that there is a sufficient number of satellites with varying orbit orientation such that a global density field can be recovered.

METHODOLOGY

The measurement in this tomography application is derived from the change in a due to drag. It is first required to write the total change in a due to all modeled perturbing acceleration, and then isolating only that due to drag. Using the Poisson brackets to derive the osculating orbit element rates from Lagrange's planetary equations,[25] the variational equation for a is

$$\frac{da}{dt} = \frac{\partial a}{\partial \mathbf{v}} \mathbf{a}_p \ , \tag{4}$$

where $\mathbf{a}_p$ is the perturbing acceleration (i.e. all accelerations other than the two-body gravitational acceleration), and

$$\frac{\partial a}{\partial \mathbf{v}} = \frac{2a^2}{\mu} \mathbf{v}^T \ . \tag{5}$$

For the present discussion, $\mathbf{a}_p$ is split into the component due to drag, $\mathbf{a}_d$, and the component due to non-drag accelerations, $\mathbf{a}_{nd}$

$$\mathbf{a}_p = \mathbf{a}_d + \mathbf{a}_{nd} \ . \tag{6}$$

The acceleration $\mathbf{a}_{nd}$ need not be specified yet, but in general these non-drag perturbations (e.g. non-spherical gravity, third-body gravity, solar radiation pressure) will be a function of position, $\mathbf{a}_{nd} = \mathbf{a}_{nd}(\mathbf{r})$. The drag acceleration is written as

$$\mathbf{a}_d(\mathbf{r}, \mathbf{v}) = -\frac{1}{2} \beta s \rho_{\mathrm{mod}} v_r \mathbf{v}_r \ , \tag{7}$$

where $\beta \equiv C_d A/m$ is the ballistic coefficient relating the satellite's drag coefficient (C_d), drag cross-sectional area (A), and mass (m); $v_r = |\mathbf{v}_r|$ is the magnitude of the wind-relative velocity

vector; and the modeled atmospheric density is related to the true atmospheric density via a correction factor $s \equiv \rho_{\text{true}}/\rho_{\text{mod}}$.

Therefore, combining Eqs. (4), (5), and (6) and integrating both sides

$$\int_{a(t_1)}^{a(t_2)} \frac{da}{a^2} = \frac{2}{\mu}\int_{t_1}^{t_2} \mathbf{v}^T \mathbf{a}_d(\mathbf{r},\mathbf{v})dt + \frac{2}{\mu}\int_{t_1}^{t_2} \mathbf{v}^T \mathbf{a}_{nd}(\mathbf{r})dt \ . \tag{8}$$

The second term on the right-hand side of Eq. (8) can be thought of as a correction factor for the non-drag perturbations

$$C_{\text{nd}}(\mathbf{r},\mathbf{v}) \equiv \frac{2}{\mu}\int_{t_1}^{t_2} \mathbf{v}^T \mathbf{a}_{nd}(\mathbf{r})dt \ . \tag{9}$$

After solving the definite integral on the left-hand side of Eq. (8) and rearranging, the result is

$$\frac{1}{a(t_2)} - \frac{1}{a(t_1)} - C_{\text{nd}}(\mathbf{r},\mathbf{v}) = -\frac{2}{\mu}\int_{t_1}^{t_2} \mathbf{v}^T \mathbf{a}_d(\mathbf{r},\mathbf{v})dt \ . \tag{10}$$

For ease of notation, define w such that

$$w(\mathbf{r}(t),\mathbf{v}(t))s(\mathbf{r}(t)) = -\frac{2}{\mu}\left[\mathbf{v}\right]^T \mathbf{a}_d(\mathbf{r},\mathbf{v}) \ , \tag{11}$$

hence w represents all quantities under the integral except s. Now rewriting the integral on the right-hand side of Eq. (10) to account for times inside the grid and outside the grid, so for points outside the grid we assume $s = 1$,

$$\frac{1}{a(t_2)} - \frac{1}{a(t_1)} - C_{\text{nd}}(\mathbf{r},\mathbf{v}) = \int_{t_{\text{in}}} w(\mathbf{r}(t),\mathbf{v}(t))s(\mathbf{r}(t))dt + \int_{t_{\text{out}}} w(\mathbf{r}(t),\mathbf{v}(t))dt \ . \tag{12}$$

The second term on the right-hand side of Eq. (12) can be thought of as another correction factor, this time for the change in a due to drag effects occurring outside of the grid

$$C_{\text{out}}(\mathbf{r},\mathbf{v}) \equiv \int_{t_{\text{out}}} w(\mathbf{r}(t),\mathbf{v}(t))dt \tag{13}$$

and rearranging

$$\frac{1}{a(t_2)} - \frac{1}{a(t_1)} - C_{\text{nd}}(\mathbf{r},\mathbf{v}) - C_{\text{out}}(\mathbf{r},\mathbf{v}) = \int_{t_{\text{in}}} w(\mathbf{r}(t),\mathbf{v}(t))s(\mathbf{r}(t))dt \ . \tag{14}$$

It is now important to distinguish which quantities are measured, assumed known, and to be solved. The semimajor axis at t_1 and t_2 are considered measured quantities, since they come from the assumed OE scheme, and are denoted as $\tilde{a}_2$ and $\tilde{a}_1$. The density scale factor s is the quantity to be solved via tomography. However, there is still dependence on $\mathbf{r}(t)$ and $\mathbf{v}(t)$ over the time span from t_1 to t_2, which are unknown. Given the initial state estimates (from the OE results) and modeled forces and assuming $s = 1$, we can numerically integrate the equations of motion to give an estimate of the position and velocity which we denote as $\mathbf{r}^*$ and $\mathbf{v}^*$. The density ρ_{mod} is dependent on the position, which is here evaluated on $\mathbf{r}^*$. Furthermore, β is not known perfectly, and thus must be assumed as β^* (e.g. via modeling[26] or prior fitting[11]).

Taking the above discussion into consideration, Eq. (14) is now written as

$$\frac{1}{\tilde{a}_2} - \frac{1}{\tilde{a}_1} - C_{\text{nd}}(\mathbf{r}^*, \mathbf{v}^*) - C_{\text{out}}(\mathbf{r}^*, \mathbf{v}^*) = \int_{t_{\text{in}}} w(\mathbf{r}^*(t), \mathbf{v}^*(t)) s(\mathbf{r}^*(t)) dt \ . \tag{15}$$

We can therefore define the net derived measurement y as the left-hand side of Eq. (15), resulting in

$$y = \int_{t_{\text{in}}} w(\mathbf{r}^*(t), \mathbf{v}^*(t)) s(\mathbf{r}^*(t)) dt \ . \tag{16}$$

Equation (16) has the form of a Fredholm integral of the first kind, where w is the kernel representing the physical relationship between the unknown model s and observed data y.[27]

Further physical insight into the quantity $1/\tilde{a}_2 - 1/\tilde{a}_1$ in Eq. (15) can be obtained by recalling the definition $\xi = -\mu/(2a)$ of the specific mechanical energy for a Keplerian orbit. By rearranging the $-2/\mu$ appearing in the definition of w in Eq. (11), then Eq. (15) can be modified such that the measured quantity in y is actually the change in the specific mechanical energy, $\xi_2 - \xi_1$, as defined by the osculating semimajor axis. This insight is useful when recalling the original tomographic inspiration: rather than measuring the decay in X-ray intensity, we are effectively measuring the decay in orbital specific mechanical energy.

The linear system in Eq. (16) is solved by first discretizing the integral and then writing in matrix form. A spatial grid with cell indices $n \in \{1, \ldots, N\}$ is defined, where $s_n = s(\mathbf{d}_n)$ and $\mathbf{d}_n$ specifies the center of cell n (also s_n is assumed uniform in each cell). For satellite $i \in \{1, \ldots, M\}$, the equations of motion are numerically propagated, with time step Δt, as described above, resulting in discrete values of $\mathbf{r}_k^*$ and $\mathbf{v}_k^*$. Here, $k \in \{K_{i,n}\}$ represents the time instances that satellite i is in cell n, and is a subset of this satellite's total propagated times. The integral in Eq. (16) is replaced by a summation by discretizing along the satellite's trajectory through the grid (Figure 3)

$$y_i = \begin{bmatrix} w_{i,1}\Delta t_{i,1} & \cdots & w_{i,N}\Delta t_{i,N} \end{bmatrix} \begin{bmatrix} s_1 & \cdots & s_N \end{bmatrix}^T \tag{17}$$

where $\Delta t_{i,n}$ is the time spent by satellite i in cell n, and $w_{i,n}$ is the averaged quantity $w(t, \mathbf{r}^*, \mathbf{v}^*)$ for satellite i in cell n, i.e.

$$w_{i,n} = \frac{1}{N_{i,n}} \sum_{k \in K_{i,n}} w(t_k, \mathbf{r}_k^*, \mathbf{v}_k^*) \tag{18}$$

where $N_{i,n}$ is the number of times satellite i is in cell n.

Using the approximation $\Delta t_{i,n} \approx N_{i,n}\Delta t$, then from Eq. (18):

$$w_{i,n}\Delta t_{i,n} \approx \Delta t \sum_{k \in K_{i,n}} w(t_k, \mathbf{r}_k^*, \mathbf{v}_k^*) \ . \tag{19}$$

For ease of notation, define

$$h_{i,n} \equiv \sum_{k \in K_{i,n}} w(t_k, \mathbf{r}_k^*, \mathbf{v}_k^*) \tag{20}$$

then the matrix form of Eq. (17) that includes all satellites M is

$$\begin{bmatrix} y_1 \\ \vdots \\ y_M \end{bmatrix} = \Delta t \begin{bmatrix} h_{1,1} & \cdots & h_{1,N} \\ \vdots & \ddots & \vdots \\ h_{M,1} & \cdots & h_{M,N} \end{bmatrix} \begin{bmatrix} s_1 \\ \vdots \\ s_N \end{bmatrix} \ . \tag{21}$$

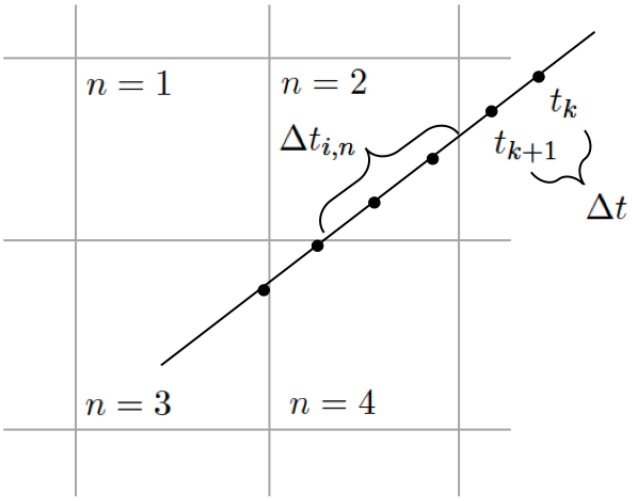

Figure 3. Illustration of grid (gray) with satellite orbit (black) propagated at finite time t_k.

Note that in general a given satellite will not pass through each cell in the grid. If a satellite does not pass through a cell, then $h_{i,n} = 0$ for that cell.

Equation (21) is then written concisely as $\mathbf{y} = H\mathbf{s}$. In general, this is an ill-posed problem because $N > M$ and the matrix H is sparse (i.e. most entries are zero). We solve this problem using Tikhonov regularization[28]

$$\underset{\mathbf{s}}{\operatorname{argmin}} \frac{1}{2}\|H\mathbf{s} - \mathbf{y}\|_2^2 + \frac{\lambda}{2}\|D\mathbf{s}\|_2^2 \,, \tag{22}$$

the solution for which can be expressed in closed-form as

$$(H^T H + \lambda D^T D)\mathbf{s} = H^T \mathbf{y} \,, \tag{23}$$

which can be solved using a variety of standard methods.[29] We choose the regularization operator D as a discretization of the 3D gradient $\nabla\mathbf{s}$ since we expect $\mathbf{s}$ to be a spatially smooth field. (We do not apply Total Variation regularization[30] since discontinuities are not expected.)

Although reasonable results are obtained using the simple gradient in Cartesian coordinates

$$\nabla s = \left(\frac{\partial s}{\partial x}, \frac{\partial s}{\partial x}, \frac{\partial s}{\partial z}\right) , \tag{24}$$

we have obtained somewhat better results using the correct gradient for the spherical coordinates in which our problem is represented

$$\nabla s = \left(\frac{\partial s}{\partial r}, \frac{1}{r}\frac{\partial s}{\partial \theta}, \frac{1}{r\sin(\theta)}\frac{\partial s}{\partial \phi}\right) \,. \tag{25}$$

For notational simplicity Eq. (22) is defined using a single regularization parameter λ, but for additional flexibility we express this problem using individual terms for each component of the gradient and allow individual regularization parameters, which we denote λ_r, λ_θ, and λ_ϕ, for each of these terms.

SIMULATION SETUP

We define a grid as follows: radial direction is 6678 to 6878 km (300 to 500 km altitude), with 100 km uniform spacing; (inertial) longitude direction is -180° to 180°, with 20° uniform spacing; (inertial) latitude direction is -90° to 90°, with 20° uniform spacing. The resulting number of grid cells is $N = 324$.

The initial ground truth Cartesian states $\mathbf{r}(t_0)$ and $\mathbf{v}(t_0)$ are generated from a random sampling of $M = 100$ satellite orbits (Figure 4) as follows. First, the radius of perigee r_p and radius of apogee r_a are sampled from a uniform distribution between two ranges, depending on whether they are categorized as low-eccentricity or high-eccentriciy. The low-eccentricity orbits have two radial distances sampled from a uniform distribution from 6703 to 6853 km (325 to 475 km altitude), where the lower of the two is set to r_p. The high-eccentricity orbits have one radial distance sampled from a uniform distribution from 6703 to 6853 km (325 to 475 km altitude), and the other radial distance is sampled from a uniform distribution from 6703 to 10378 km (325 to 4000 km altitude). The initial semimajor axis a_0 and eccentricity e_0 then follow from $a_0 = (r_p + r_a)/2$ and $e_0 = (r_a - r_p)/(r_a + r_p)$. The initial elements i_0, Ω_0, ω_0, and f_0 are all sampled from a uniform distribution from 0 to 2π rad. These initial osculating Keplerian elements are then converted to $\mathbf{r}(t_0)$ and $\mathbf{v}(t_0)$. In this simulation, we do not specify any actual ground sites for tracking, and instead for simplicity assume that the orbits are measured at t_0, and again 5 orbital revolutions later (i.e. ≈ 8.5 hours).

Each satellite is propagated twice. One propagation represents the ground-truth, where the force model parameters are known. The other propagation represents the assumed trajectory $(\mathbf{r}^*, \mathbf{v}^*)$, where some of the force model parameters are changed slightly from ground-truth (e.g. to simulate our imperfect knowledge of β), and where $[\mathbf{r}^*(t_1), \mathbf{v}^*(t_1)]$ are slightly in error compared with $[\mathbf{r}(t_1), \mathbf{v}(t_1)]$ to simulate the OE errors (and similarly at t_2). The OE errors are assumed to be Gaussian with 5 m (1σ) position and 1 mm/s (1σ) velocity variance in each Cartesian component, as well as having β knowledge errors of 5% (1σ).

The numerical propagator is a special perturbations propagator using Cowell's formulation with the Cartesian position and velocity. For the Earth's nonuniform gravity, it uses a 7x7 spherical harmonic expansion with the EGM96 coefficients. Also included are third-body effects from the Sun and Moon, and solar radiation pressure accelerations (where these force model parameters are assumed known). The GITM model[31] is used in our simulations to represent the true density ρ_{true}, and the MSIS model[32] is used as the modeled density ρ_{mod}. The current simulation assumes no winds for both the ground-truth and the reference orbits $(\mathbf{r}^*, \mathbf{v}^*)$, and instead uses a simple co-rotating atmosphere model in the calculation of $\mathbf{v}_r$.

SIMULATION RESULTS

Figure 5 shows the time-average of the true $s = \rho_{\text{true}}/\rho_{\text{mod}}$ value, evaluated over the same grid as defined above, where a slice is taken at 350 km altitude. Figure 6 shows the corresponding slice of the estimated s field, using $\lambda_\theta = 1 \times 10^{-17}$, $\lambda_\phi = 1 \times 10^{-17}$, and $\lambda_r = 1 \times 10^{-12}$. We see that overall there is good agreement between the two: the "bulge" of $s \approx 0.9$ is apparent in both figures centered around 0 deg latitude and -100 deg longitude, and the rest of the field is matching near $s \approx 0.7$. However, there are some finer structures apparent in Figure 5 that are not quite visible in Figure 6. Figures 7 and 8 show the corresponding results for the slice at 450 km altitude, and the overall results are the same. The RMS error over the entire 3-D grid between the time-averaged ground-truth s and the estimated s was 0.07 (unit-less).

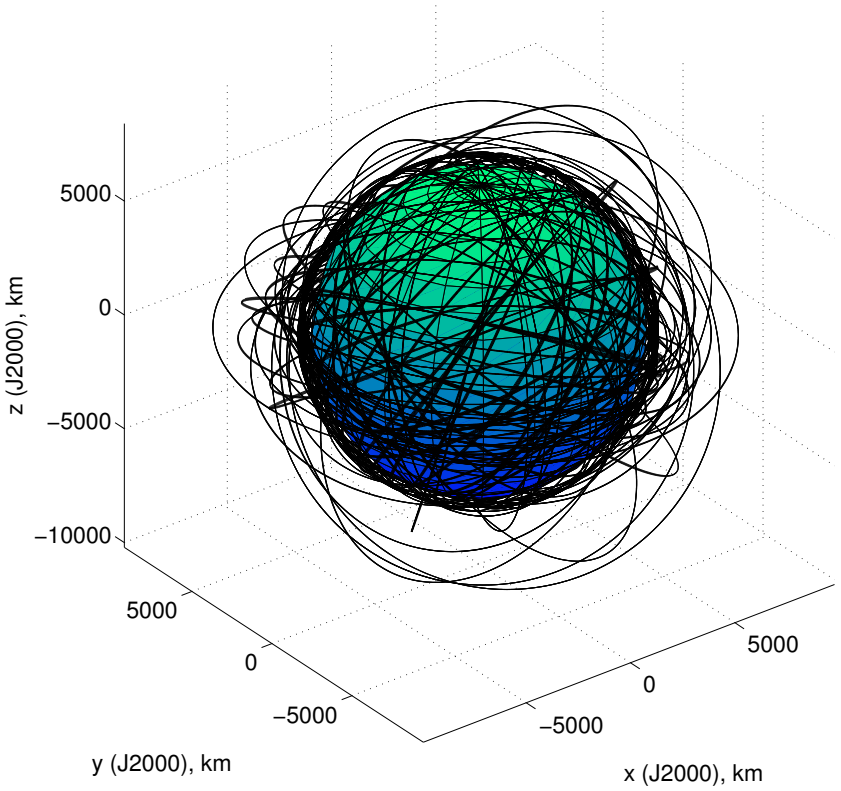

Figure 4. Simulated random orbits, $M = 100$ satellites.

DISCUSSION

Considering the RMS error of 0.07 in s mentioned above, and that the nominal value for the true s is around 1, then the true time-averaged density can be reconstructed using our estimated s to within approximately 10%. Of course, we must also consider that the true density will also have small variations in time relative to the time-averaged value, so that there would be some additional errors if we were to compare our estimated time-average s with the instantaneous true density. For example, in the simulation scenario discussed above, the instantaneous density varied only by a few percent relative to the time-averaged value. However, addition simulations will have to be performed in future work to ensure that the tomography method described here would also be feasible in cases where the instantaneous density varies greatly about its time-averaged value.

The density reconstruction method described in this paper has some practical advantages over existing methods. Unlike a weighted least squares approach where the orbit states and density corrections are estimated simultaneously from tracking data (e.g. like HASDM's approach), where the partial derivatives of the system dynamics and measurements with respect to the state must be found, our method requires no such partial derivatives. Likewise, no effort needs to be spent on parameterizing the density model corrections to allow them to be easily estimated along with

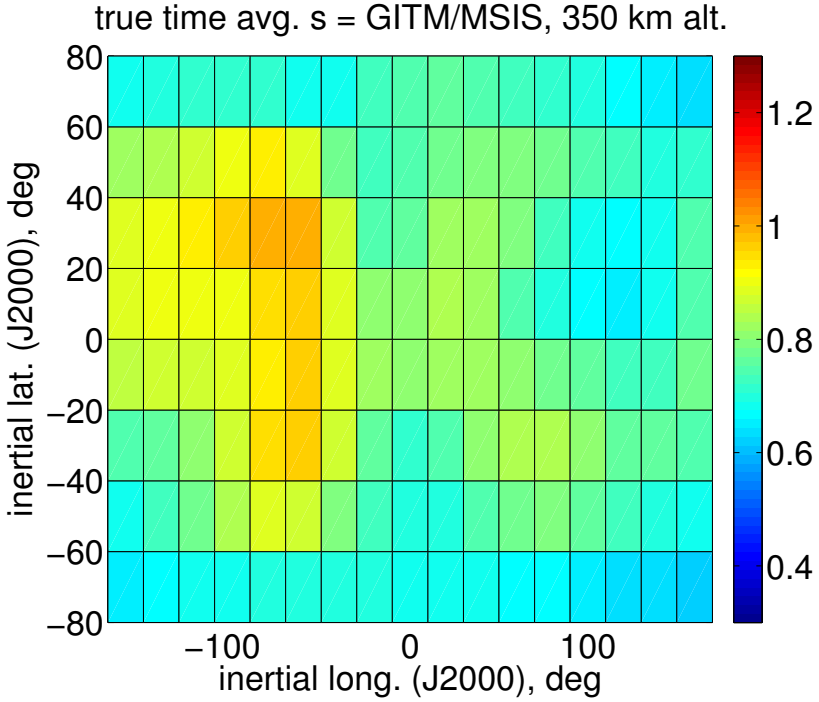

Figure 5. True time-averaged $s = \rho_{\mathrm{true}}/\rho_{\mathrm{mod}}$, slice at 350 km alt.

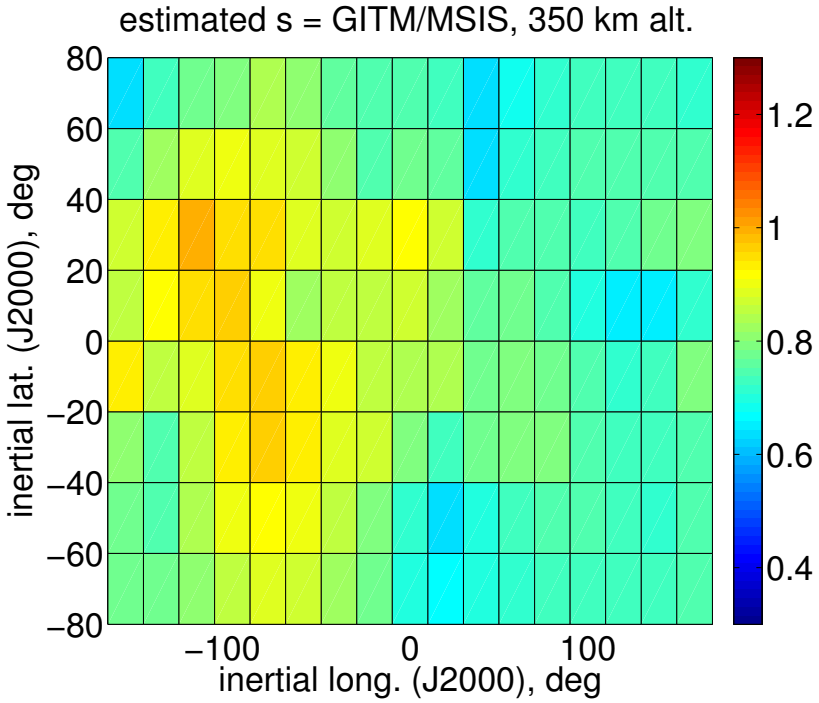

Figure 6. Estimated time-averaged $s = \rho_{\mathrm{true}}/\rho_{\mathrm{mod}}$, slice at 350 km alt.

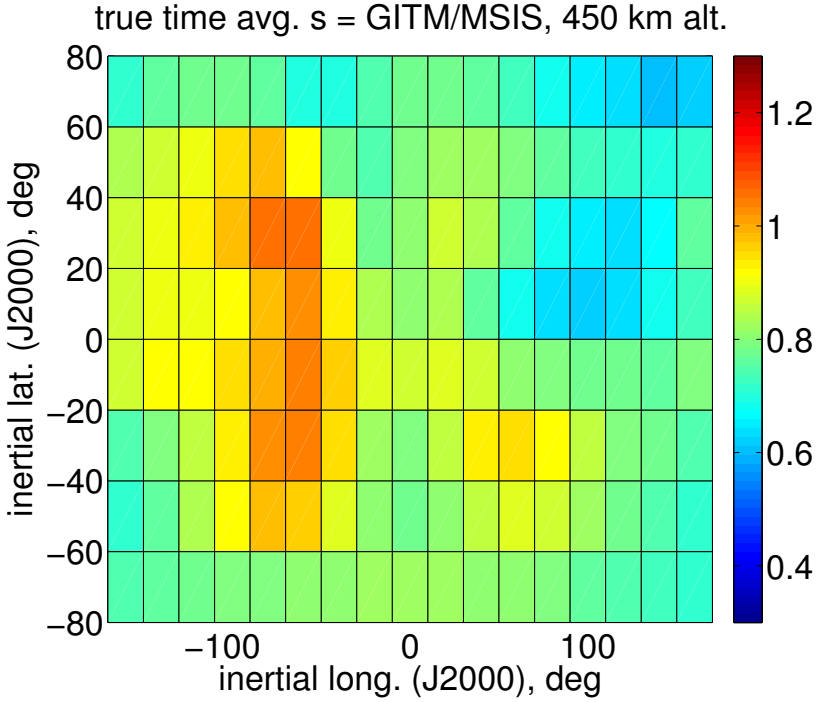

Figure 7. True time-averaged $s = \rho_{\mathrm{true}}/\rho_{\mathrm{mod}}$, slice at 450 km alt.

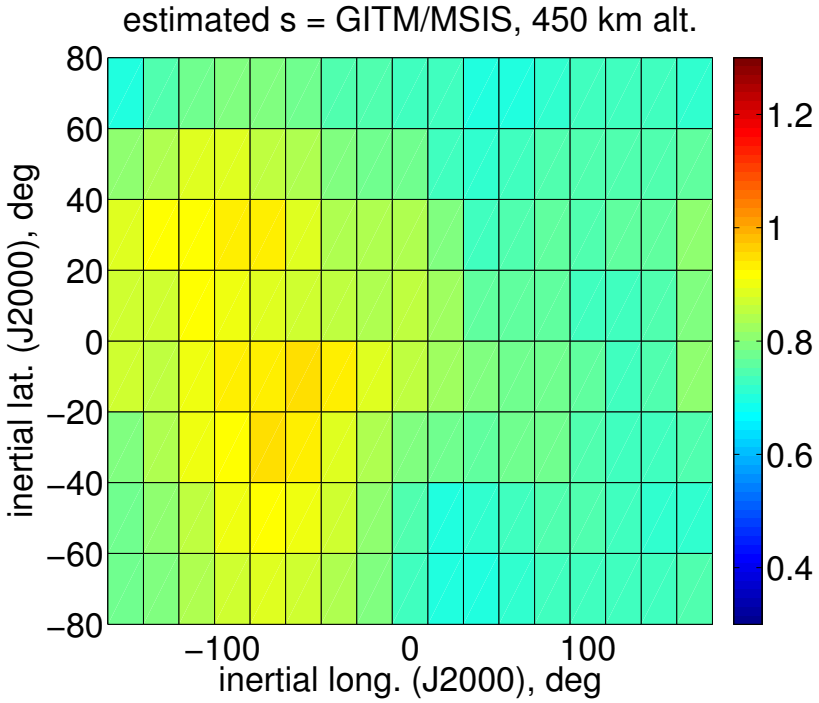

Figure 8. Estimated time-averaged $s = \rho_{\mathrm{true}}/\rho_{\mathrm{mod}}$, slice at 450 km alt.

the orbits. For example, Hinks and Psiaki[33] used a unique spline-based density parameterization for another study of density estimation using telemetry from a cross-linked constellation like Iridium. In fact, our method is essentially density-model-agnostic: given a function that describes the modeled density ρ_{mod} as a function of position and time, it is trivial to use this function in the numerical evaluation of the term w that appears in Eqs. (13) and (16). Furthermore, it is straightforward to change the desired resolution of the estimated s field by simply changing the grid spacing. This is analogous to using a higher degree and order spherical harmonic expansion, if we were to use such an expansion to parameterize the density corrections. Lastly, assuming we are satisfied with the time-averaged density estimate between t_1 and t_2, we have demonstrated that we can sufficiently reconstruct this density using only the measured orbit states at t_1 and t_2, rather than requiring tracking data between those times.

There are several areas where the simulation fidelity could have been improved in this study, e.g. we assumed perfect knowledge of winds and solar radiation pressure force model parameters. Future studies will be required to verify that we can achieve similarly feasible results when uncertainty in these effects are also included. Additionally, we considered only the aerodynamic drag forces (i.e. in the direction of the relative velocity) and ignored aerodynamic forces perpendicular to the relative velocity direction (i.e. lift and side forces). For general studies on the effects of the atmosphere on satellite motion, it is common to assume (e.g. Ref. 34) that the effects of lift and side forces on the orbit will be small compared to those of drag. This result is due to the blunt or irregular shape of most space objects, and the fact that the direction of these forces may vary widely over an orbital revolution and thus tend to average out. However, these other forces cannot be ignored for detailed studies using precise measurements such as accelerometers (e.g. Ref. 10).

CONCLUSIONS

This paper has introduced a new tomography-based method to reconstruct the atmospheric density, which uses satellite orbital states as measurements. This method allows the use of temporally-sparse measurements (e.g. ground-based tracking) to find a time-averaged, yet spatially resolved, global density correction. Because the density corrections are in the form of scale factor adjustments to an assumed density model, it is straightforward to substitute any number of desired density models into the formulation. Based on the initial feasibility study performed in this paper, the method requires a number of satellites (~ 100) in spatially diverse orbits and with well-known drag properties (e.g. ballistic coefficient). However, this requirement on the tracking targets is similar in principle to existing methods like the U.S. Air Force's HASDM method. The simulation results show that the time-averaged density over ~ 8.5 hours can be reconstructed to within $\sim 10\%$. Further feasibility studies are required to ensure that this method can be applied to increasingly realistic scenarios, and eventually actual observational data.

ACKNOWLEDGMENTS

This work was conducted under the auspices of the U.S. Department of Energy, with support from the Los Alamos National Laboratory (LANL) Directed Research and Development program. We thank Humberto Godinez and Andrew Walker of LANL for generating the GITM and MSIS atmospheric density data used in this study. We also thank David Palmer of LANL for motivating the insight regarding the specific mechanical energy of the orbit.

NOTATION

A	drag cross-sectional area, km^2
a	semimajor axis, km
$\mathbf{a}_d$	drag acceleration vector, km/s^2
$\mathbf{a}_{nd}$	non-drag acceleration vector, km/s^2
$\mathbf{a}_p$	perturbing acceleration vector, km/s^2
C_d	drag coefficient, unitless
D	discretized regularization operator
$\mathbf{d}$	position vector of cell, km
e_0	initial eccentricity
f	X-ray attenuation coefficient
f_0	initial true anomaly, rad
H	linear measurement matrix
h	summed kernel, km^{-1} s^{-1}
i	satellite index
i_0	initial inclination, rad
K	set of times in a given cell
k	discrete time index
I	X-ray intensity
M	number of satellites
m	mass, kg
N	number of cells in grid
n	cell index
$\mathbf{r}$	position vector of satellite, km
r	radial direction, km
r_a	radius of apogee, km
r_p	radius of perigee, km
$\mathbf{s}$	vector of density model scale factors, unitless
s	density model scale factor, unitless
t	time, s
$\mathbf{v}$	inertial velocity vector, km/s
$\mathbf{v}_r$	wind-relative velocity vector, km/s
w	kernel, km^{-1} s^{-1}
x	generalized distance
$\mathbf{y}$	measurement vector, km^{-1}
y	net derived measurement, km^{-1}
β	drag ballistic coefficient, km^2/kg
θ	latitude, rad
λ	smoothness constraint
μ	Earth gravitational parameter, km^3/s^2
ξ	orbit specific mechanical energy, km^2/s^2
ρ_{mod}	modeled density, kg/km^3
ρ_{true}	true density, kg/km^3
ϕ	longitude, rad
Ω_0	initial right-ascension of the ascending node, rad
ω_0	initial argument of perigee, rad

REFERENCES

[1] F. A. Marcos, "Accuracy of atmospheric drag," *Advances in Space Research*, Vol. 10, No. 3, 1990, pp. 417–422, doi:10.1016/0273-1177(90)90381-9.

[2] F. A. Marcos, J. O. Wise, M. J. Kendra, and N. Grossbard, "Satellite Drag Research: Past, Present and Future," *Advances in the Astronautical Sciences*, AAS, 2003, pp. 1865–1878.

[3] D. Vallado and D. Finkleman, "A Critical Assessment of Satellite Drag and Atmospheric Density Modeling," 2010. AIAA Paper 2008-6442, doi:10.2514/6.2008-6442.

[4] C. A. McLaughlin, A. Hiatt, and T. Lechtenberg, "Precision Orbit Derived Total Density," *Journal of Spacecraft and Rockets*, Vol. 48, Jan. 2011, pp. 166–174, doi:10.2514/1.47624.

[5] E. Doornbos and H. Klinkrad, "Modelling of space weather effects on satellite drag," *Advances in Space Research*, Vol. 37, Jan. 2006, pp. 1229–1239, doi:10.1016/j.asr.2005.04.097.

[6] A. C. Nicholas, J. M. Picone, S. E. Thonnard, R. R. Meier, K. F. Dymond, and D. P. Drob, "A methodology for using optimal MSIS parameters retrieved from SSULI data to compute satellite drag on LEO objects," *Journal of Atmospheric and Solar-Terrestrial Physics*, Vol. 62, 2000, pp. 1317–1326, doi:10.1016/S1364-6826(00)00105-X.

[7] S. Bruinsma and R. Biancale, "Total Densities Derived from Accelerometer Data," *Journal of Spacecraft and Rockets*, Vol. 40, No. 2, 2003, doi:10.2514/2.3937.

[8] E. K. Sutton, J. Forbes, and R. Nerem, "Global thermospheric neutral density and wind response to the severe 2003 geomagnetic storms from CHAMP accelerometer data," *Journal of Geophysical Research*, Vol. 110, No. A9, 2005, pp. 1–10, doi:10.1029/2004JA010985.

[9] S. L. Bruinsma and J. M. Forbes, "Storm-Time Equatorial Density Enhancements Observed by CHAMP and GRACE," *Journal of Spacecraft and Rockets*, Vol. 44, Nov. 2007, pp. 1154–1159, doi:10.2514/1.28134.

[10] E. Doornbos, J. V. Den Ijssel, H. Luehr, M. Foerster, and G. Koppenwallner, "Neutral Density and Crosswind Determination from Arbitrarily Oriented Multiaxis Accelerometers on Satellites," *Journal of Spacecraft and Rockets*, Vol. 47, July 2010, pp. 580–589, doi:10.2514/1.48114.

[11] B. R. Bowman, "True Satellite Ballistic Coefficient Determination for HASDM," *AIAA/AAS Astrodynamics Specialist Conference, Aug. 2002, Monterey, CA*, 2002. AIAA Paper 2002-4887, doi:10.2514/6.2002-4887.

[12] B. R. Bowman and M. F. Storz, "Time Series Analysis of HASDM Thermospheric Temperature and Density Corrections," *AIAA/AAS Astrodynamics Specialist Conference, Aug. 2002, Monterey, CA*, 2002. AIAA Paper 2002-4890, doi:10.2514/6.2002-4890.

[13] M. F. Storz, "HASDM Validation Tool Using Energy Dissipation Rates," *AIAA/AAS Astrodynamics Specialist Conference, Aug. 2002, Monterey, CA*, 2002. AIAA Paper 2002-4889, doi:10.2514/6.2002-4889.

[14] M. F. Storz, B. R. Bowman, M. J. I. Branson, S. J. Casali, and W. K. Tobiska, "High accuracy satellite drag model (HASDM)," *Advances in Space Research*, Vol. 36, No. 12, 2005, pp. 2497–2505, doi:10.1016/j.asr.2004.02.020.

[15] S. J. Casali, W. N. Barker, and B. R. Bowman, "Improvements in Density Modeling Using the Air Force Dynamic Calibration Atmosphere Model," *AIAA/AAS Astrodynamics Specialist Conference, Aug. 2006*, 2006. AIAA paper 2006-6168, doi:10.2514/6.2006-6168.

[16] E. K. Sutton, S. B. Cable, C. S. Lin, and F. A. Marcos, "Improved basis functions for dynamic calibration of semi-empirical thermospheric models," *Advanced Maui Optical and Space Surveillance Technologies Conference Paper, Sep. 2011, Maui, Hawaii*, 2011.

[17] N. L. Johnson, "U.S. Space Surveillance," *Advances in Space Research*, Vol. 13, Aug. 1993, pp. 5–20, doi:10.1016/0273-1177(93)90563-Q.

[18] J. C. Santamarina and D. Fratta, *Discrete Signals and Inverse Problems: An Introduction for Engineers and Scientists*, ch. 8. John Wiley and Sons, 1 ed., 2005.

[19] F. Natterer, *The Mathematics of Computerized Tomography*, ch. 1. Philadelphia: Society of Industrial and Applied Mathematics, 2001.

[20] H. Fleming, "Satellite Remote Sensing by the Technique of Computed Tomography," *Journal of Applied Meteorology*, Vol. 21, 1982, pp. 1538–1549.

[21] M. Gorbunov, "Three-dimensional satellite refractive tomography of the atmosphere : Numerical simulation," *Radio Science*, Vol. 31, No. 1, 1996, pp. 95–104.

[22] P. Bernhardt, C. Selcher, S. Basu, G. Bust, and S. Reising, "Atmospheric Studies with the Tri-Band Beacon Instrument on the COSMIC Constellation," *TAO*, Vol. 11, No. 1, 2000, pp. 291–312.

[23] A. Flores, L. P. Gradinarsky, P. Elosegui, G. Elgered, J. Davis, and A. Rius, "Sensing atmospheric structure : Tropospheric tomographic results of the small-scale GPS campaign at the Onsala Space Observatory," *Earth Planets Space*, Vol. 52, No. 1999, 2000, pp. 941–945.

[24] A. Doicu, T. R. Trautmann, and F. Schreier, *Numerical Regularization for Atmospheric Inverse Problems*, ch. 1, pp. 4 – 8. Springer-Verlag, 2010.

[25] H. Schaub and J. L. Junkins, *Analytical Mechanics of Space Systems*, ch. 12, p. 513. AIAA, 2003.

[26] P. M. Mehta, A. Walker, C. McLaughlin, and J. Koller, "Comparing Physical Drag Coefficients Computed with Direct Simulation Monte Carlo Using Different Gas-Surface Interaction Models," *Journal of Spacecraft and Rockets*, submitted Dec. 2012.

[27] R. C. Aster, B. Borchers, and C. H. Thurber, *Parameter Estimation and Inverse Problems*, ch. 1, p. 14. Academic Press, 2011.

[28] A. N. Tikhonov and V. Y. Arsenin, *Solutions of Ill-Posed Problems*. New York, NY, USA: Wiley, 1977.

[29] G. H. Golub and C. F. Van Loan, *Matrix computations*. Johns Hopkins University Press, 3 ed., 1996.

[30] L. Rudin, S. J. Osher, and E. Fatemi, "Nonlinear total variation based noise removal algorithms.," *Physica D. Nonlinear phenomena*, Vol. 60, November 1992, pp. 259–268, doi:10.1016/0167-2789(92)90242-f.

[31] A. J. Ridley, Y. Deng, and G. Toth, "The global ionosphere-thermosphere model," *Journal of Atmospheric and Solar-Terrestrial Physics*, Vol. 68, May 2006, pp. 839–864, doi:10.1016/j.jastp.2006.01.008.

[32] J. M. Picone, A. E. Hedin, D. P. Drob, and A. C. Aikin, "NRLMSISE-00 empirical model of the atmosphere: Statistical comparisons and scientific issues," *Journal of Geophysical Research*, Vol. 107, No. A12, 2002, p. 1468, doi:10.1029/2002JA009430.

[33] J. C. Hinks and M. L. Psiaki, "Simultaneous Orbit and Atmospheric Density Estimation for a Satellite Constellation," 2010. AIAA Paper 2010-8258.

[34] D. King-Hele, *Satellite Orbits in an Atmosphere*, ch. 2, p. 21. Blackie, London, 1987.